



Sandwich nanostructured LiMnPO₄/C as enhanced cathode materials for lithium-ion batteries

Xudong Hu¹, Xiaohong Sun^{1,*}, Ming Yang¹, Huiming Ji¹, Xiaolei Li¹, Shu Cai¹, Ruisong Guo¹, Feng Hou¹, Chunming Zheng^{2,*}, and Wenbin Hu¹

¹ School of Materials Science and Engineering, Key Laboratory of Advanced Ceramics and Machining Technology of Ministry of Education, Tianjin University, Tianjin 300072, People's Republic of China

² State Key Laboratory of Hollow-Fiber Membrane Materials and Membrane Processes, School of Environmental and Chemical Engineering, Tianjin Polytechnic University, Tianjin 300387, People's Republic of China

Received: 10 July 2016

Accepted: 15 September 2016

Published online:

23 September 2016

© Springer Science+Business Media New York 2016

ABSTRACT

An alternate nanosheet/nanoparticle sandwich nanostructured LiMnPO₄ cathode material is successfully synthesized by solvothermal process using oleic acid as the chelating agent. The size of the nanoparticles is as small as ca. 20 nm, which is important to avoid the agglomeration of the nanosheets from overlapping. The carbon-coated LiMnPO₄ cathode delivers discharge capacities of 164.9 mAh g⁻¹ at 0.05 C, 159.6 mAh g⁻¹ at 0.1 C, 142.5 mAh g⁻¹ at 0.2 C, and even 77.6 mAh g⁻¹ at 5 C rates, which values are obviously better than those of the counterparts of pure nanosheets. The rate capability and cycle life tests indicate that the sandwich nanostructured LiMnPO₄/C cathode material also exhibits an excellent rate and cycle performance. The scanning electron microscopy, transmission electron microscopy, and N₂ adsorption-desorption results confirm that the sandwich nanostructured LiMnPO₄ with better dispersibility, higher surface area, and broader mesoporous distribution is beneficial to achieve the uniform post carbon-coating morphology and result in the improved electrochemical property. The enhanced electrochemical performances of sandwich nanostructured LiMnPO₄/C electrode have also been verified by the electrochemical impedance spectra and electron energy loss spectroscopy.

Introduction

With the increasing energy storage demands globally for the portable electronics, electric vehicle, and smart grid applications, the production of safe and cheap

lithium-ion batteries (LIBs) with high energy and power densities and long cycle life has attracted the significant focus and still remains a great challenge [1–3]. Ever since the first report by Goodenough and co-workers [4], olivine lithium transition-metal phosphates, LiMPO₄ (M = Fe and Mn), have

Address correspondence to E-mail: sunxh@tju.edu.cn; zhengchunming@tjpu.edu.cn

attracted much increased interest and been considered as promising candidates for replacement of Co-based cathode materials due to their low cost, non-toxicity, and large theoretical capacity [5–8]. The existence of the strong covalent bonds of $(\text{PO}_4)^{3-}$ tetrahedral polyanion in olivine structure endows LiMPO_4 ($M = \text{Fe}$ and Mn) with excellent structural stability and consequently a superior cycling performance as cathode material [9–13]. The nanoscale and carbon-coated LiFePO_4 cathode materials have been commercialized successfully for plug-in hybrid vehicles and exhibit a discharge capacity close to its theoretical value of 170 mAh g^{-1} [14, 15]. Among the phospho-olivines, LiMnPO_4 has also been extensively investigated owing to its higher redox potential of 4.1 V versus Li/Li^+ resulting in a competitive specific energy of 701 Wh kg^{-1} ($171 \text{ mAh g}^{-1} \times 4.1 \text{ V}$) compared to that of LiFePO_4 ($586 \text{ Wh kg}^{-1} = 170 \text{ mAh g}^{-1} \times 3.45 \text{ V}$) [16, 17]. Besides, LiMnPO_4 with operating voltage of 4.1 V is compatible with the commercial electrolyte system for the oxide cathode materials unlike high potential olivine cathodes of LiCoPO_4 (4.8 V) and LiNiPO_4 (5.1 V) [10, 18].

However, the low electronic conductivity ($3 \times 10^{-9} \text{ S cm}^{-1}$ at $300 \text{ }^\circ\text{C}$) and poor ionic diffusivity of LiMnPO_4 arising from the intrinsic Jahn–Teller distortion and the interface strain during charging and discharging processes impose restrictions to achieving the high electrochemical activities [9–22]. Similar to LiFePO_4 , the poor electronic and ionic conductivity issue could be overcome by the synthesis of nanoscale powders and the coating of conductive layer [23, 24]. Various routes have been used to synthesize the nanostructured LiMnPO_4 and LiMnPO_4/C composites with improved performance, such as sol–gel method [25], solvothermal method [26, 27], polyol method [16, 28], pyrolysis method [29], hydrothermal method [30], microwave method [31], precipitation method [32, 33], etc.

Even though reducing particle size may produce some adverse effects such as decrease of tap density for electrode and aggravation of side reaction between active material and electrolyte [15], construction of nanostructure has been considered as the most useful way to improve the ionic diffusivity and electrochemical performance of electrode materials, including cathode materials and anode materials [34–37]. This is because nanostructure with high surface area and small particle dimension allows the electrolyte to disperse into all the exposed surfaces,

shortens the ionic diffusion distance, and enhances the effective electrochemical reaction [10, 38, 39]. A large number of research groups have also focused on reducing the particle size of LiMnPO_4 to improve their electrode performance. Delacourt and co-workers synthesized LiMnPO_4 particles with diameters of ca. 100 nm and better discharge capacity than that of the LiMnPO_4 microparticles [32]. Rangappa et al. confirmed the size-dependent effect of LiMnPO_4 electrode [40]. Particles with diameter of ca. 20 nm displayed the best lithium storage properties. However, due to the intrinsic high surface energy and low thermodynamic stability for nanostructured materials, agglomeration will happen inevitably during the preparation of nanostructured materials [41, 42]. Some previous researches have indicated that nano-sized LiMnPO_4 would suffer from limited surface area, increasing secondary particle size, and extended ionic diffusion path, which would lead to the post nonuniform carbon-coating and poor electrochemical performance [27, 43, 44]. Therefore, the design and the synthesis of novel nanostructured LiMnPO_4 avoiding unnecessary agglomeration to improve their electrochemical performance are crucial.

In this work, we show that the electrochemical performance of LiMnPO_4/C cathode can be improved by the construction of alternate sandwich nanostructure avoiding unnecessary agglomeration. In comparison with other similar solvothermal syntheses of LiMnPO_4 nanosheet, oleic acid as chelating agent in solvothermal process led to the nucleation and subsequent growth of some LiMnPO_4 phase in a controlled manner, resulting in the existence of some spheroidal nanoparticles. In this work, proper amount of oleic acid was used to achieve the nanosheet/nanoparticle alternate sandwich nanostructure using the solvothermal synthesis method. Such a novel sandwich nanostructure offers the following advantages: (a) agglomeration phenomenon effectively avoided by the sandwich nanostructure design, (b) larger surface area exposing more insertion/extraction sites, (c) better dispersibility facilitating enhanced electrolyte contact, (d) improved ionic diffusivity owing to the shorter lithium-ion diffusion path, and (e) more uniform post carbon coating increasing the electronic conductivity. The as-synthesized alternate sandwich nanostructured LiMnPO_4/C delivers lithium storage performance of 164.9 mAh g^{-1} at 0.05 C rate, which is superior to the similar works of other groups who prepared

LiMnPO₄ nanosheet using other techniques [27, 28, 31, 40, 43]. The mechanism of the effect of sandwich nanostructure on the physicochemical and electrochemical performances of LiMnPO₄/C was extensively studied.

Experimental section

LiOH·H₂O, MnSO₄·H₂O, and H₃PO₄ were used as starting materials in a molar ratio of 3:1:1.25. Oleic acid and ethylene glycol (EG) were applied as chelating and main solvent agents, respectively. Solutions of LiOH in EG and H₃PO₄ in EG were prepared separately by adding 0.06 mol LiOH H₂O and 0.025 mol H₃PO₄ in 80 and 40 mL EG, respectively. For the preparation of MnSO₄ solution, 0.02 mol MnSO₄·H₂O was dissolved in 10 mL deionized water followed by the addition of 70 mL EG under stirring. In the preparation process of precursor, H₃PO₄ solution was added to LiOH solution very slowly under vigorous stirring. A white suspension was formed after this neutralization reaction. Then, MnSO₄ solution was slowly introduced into the white suspension under stirring throughout. Afterward, oleic acid was added into the mixture. Ethylene glycol and oleic acid were mixed in a volume ratio of 10:1. After stirring for half an hour, the obtained mixtures were transferred to a 100 mL Teflon-lined stainless steel autoclave. The solvothermal process was carried out at 200 °C for 6 h. Afterward, the as-prepared white precipitate (named LMP-S) was collected by centrifugation, repeatedly washed by deionized water and ethanol, and dried at 60 °C overnight. In contrast, LMP-N was used to stand for the samples prepared using the similar solvothermal synthesis method as LMP-S but without the addition of oleic acid.

LiMnPO₄/C samples were synthesized by adding the as-synthesized LiMnPO₄ into the glucose solution with a molar ratio of 2:1 for LiMnPO₄ and glucose. After sonicating for 1 h, the suspension was dried at 60 °C overnight. Then, the dried LiMnPO₄/glucose composite was heated at 600 °C for 5 h under Ar gas flow to synthesize the carbon-coated LiMnPO₄ samples.

The as-synthesized samples were studied by X-ray diffraction (XRD, Rigaku D/max 2500) utilizing Cu K α radiation. Typically, the data were collected from 10° to 50°. The morphology and particle size of the

samples were observed by scan electron microscopy (SEM, Hitachi, S4800), transmission electron microscopy (TEM, FEI Tecnai G2 F20), and high-resolution transmission electron microscopy (HRTEM, FEI Tecnai G2 F20). All samples subjected to TEM measurements were ultrasonically dispersed in alcohol and drop-cast onto copper grids. The surface area and pore size distribution were estimated by N₂ adsorption measurement (NOVA 2200e, Quantachrome Instruments). The samples were outgassed at 180 °C overnight before measurements were made. The surface area was obtained by the Brunauer–Emmett–Teller (BET) method, and the pore size distribution was calculated from the desorption branch of the isotherm using the Barrett–Joyner–Halanda (BJH) method. The percentage (wt%) of carbon in LMP-N/C and LMP-S/C was estimated using a thermogravimetric system (Netzsch STA449C) under a dry flowing air environment at a heating rate of 10 °C min⁻¹.

Electrochemical properties of the samples were assessed using CR2032 coin-type cells. The cathodes were made by mixing active material, super P, and polyvinylidene fluoride (PVDF) in a weight ratio of 8:1:1 in N-methyl pyrrolidinone. After stirring, the obtained slurries were coated on aluminum foil using an H-coating machine. The typical loading of the cathode with a diameter of 1.3 cm was about 2.3 mg of active materials. 1 M LiPF₆ in ethylene carbonate (EC) and dimethyl carbonate (DMC) (1:1 in volume) were used as the electrolytes. All cells were assembled in an argon-filled glove box with lithium metal as the anode. The cyclic voltammogram (CV) curve was performed between 2.0 and 4.5 V using the Electrochemical Workstation (CHI660C, Chenhua Instrument Company, China) at a scan rate of 0.1 mV s⁻¹. The electrochemical impedance spectroscopy (EIS) measurement was carried out in a frequency range from 0.1 Hz to 10⁵ Hz at a voltage amplitude of 5 mV using the same facility. EIS tests were measured on the cells after CV test. Charge–discharge tests were carried out on Land CT2001A cycler between 2.0 and 4.5 V at 25 °C according to the following procedure: charging to 4.5 V galvanostatically at 0.05, 0.1, 0.2, 0.5, 1, 2, and 5 C, respectively; charging at the constant voltage mode of 4.5 V until the current decays to one-third of each rate; and discharging galvanostatically to 2.0 V at the above-mentioned different rates. The charged electrodes were removed from the cells and rinsed several times

with absolute ethanol to remove the binder and electrolyte salt. The lithium element distribution in the charged LiMnPO_4 electrodes was then directly analyzed by Electron Energy-loss spectroscopy (EELS, FEI Tecnai G2 F20). The energy resolution of less than 0.2 eV was used. A scanning analysis was implemented to prepare the lithium element maps.

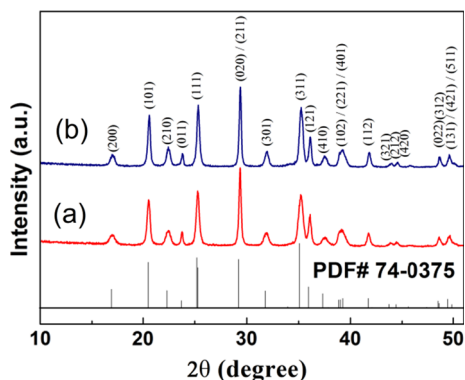


Figure 1 XRD patterns of (a) LMP-N and (b) LMP-S.

Results and discussion

Figure 1 shows the XRD patterns of the solvothermal synthesized samples with or without the adding of oleic acid. All the diffractions could be indexed to the olivine-type LiMnPO_4 with a $Pmnb$ space group of the orthorhombic system (JCPDS card No. 74-0375). No other impurity phase was observed. For both the samples, the peak intensity of (020) ($I_{(020)}$) is the highest, which indicates that crystal growth of the obtained samples occurs along the b-axis. Figure 2 shows the SEM images of LMP-N and LMP-S. From Fig. 2a, b, we can see that LMP-N consists of pure nanosheet crystals with length and width in the range of 100–200 nm and thickness of about 20 nm. Obviously, the nanostructured LMP-N samples aggregate extensively with the surface conglutination of nanosheets, which is supposed to be harmful for the effective exposure of active surface and decreases the diffusion and insertion/extraction speed of lithium ion for LIBs. In contrast, when oleic acid was added as chelating agent for the synthesis of LMP-S, an

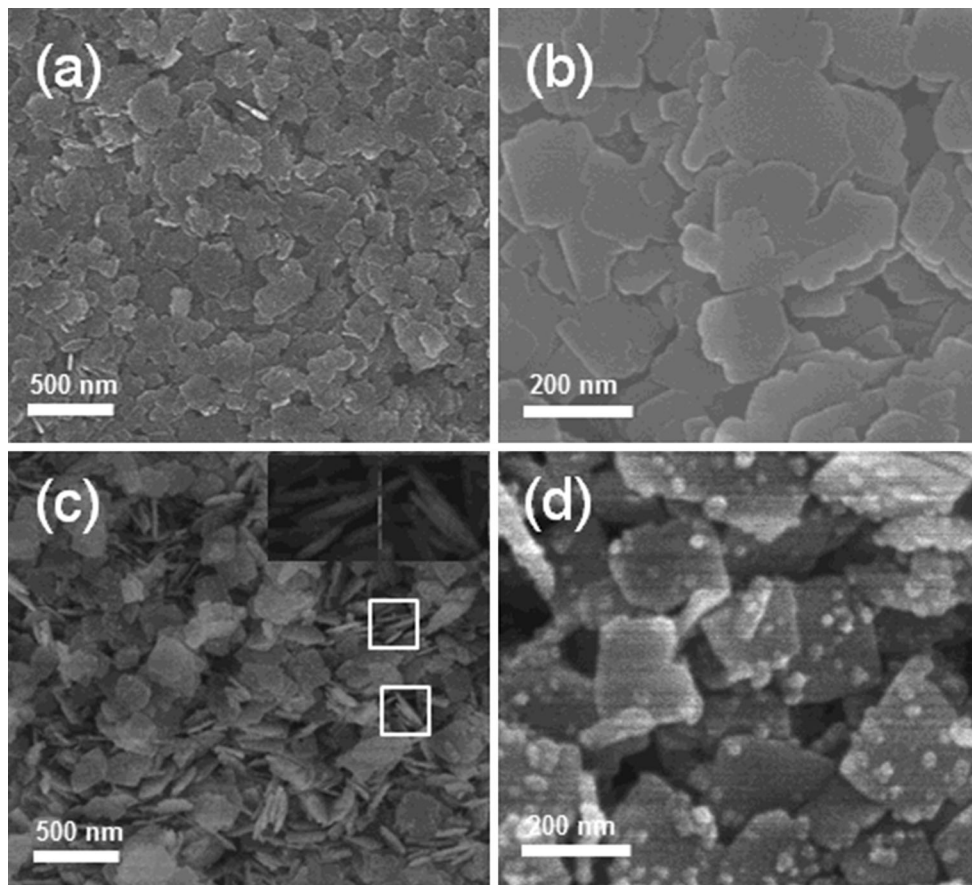


Figure 2 SEM images of a, b LMP-N and c, d LMP-S.

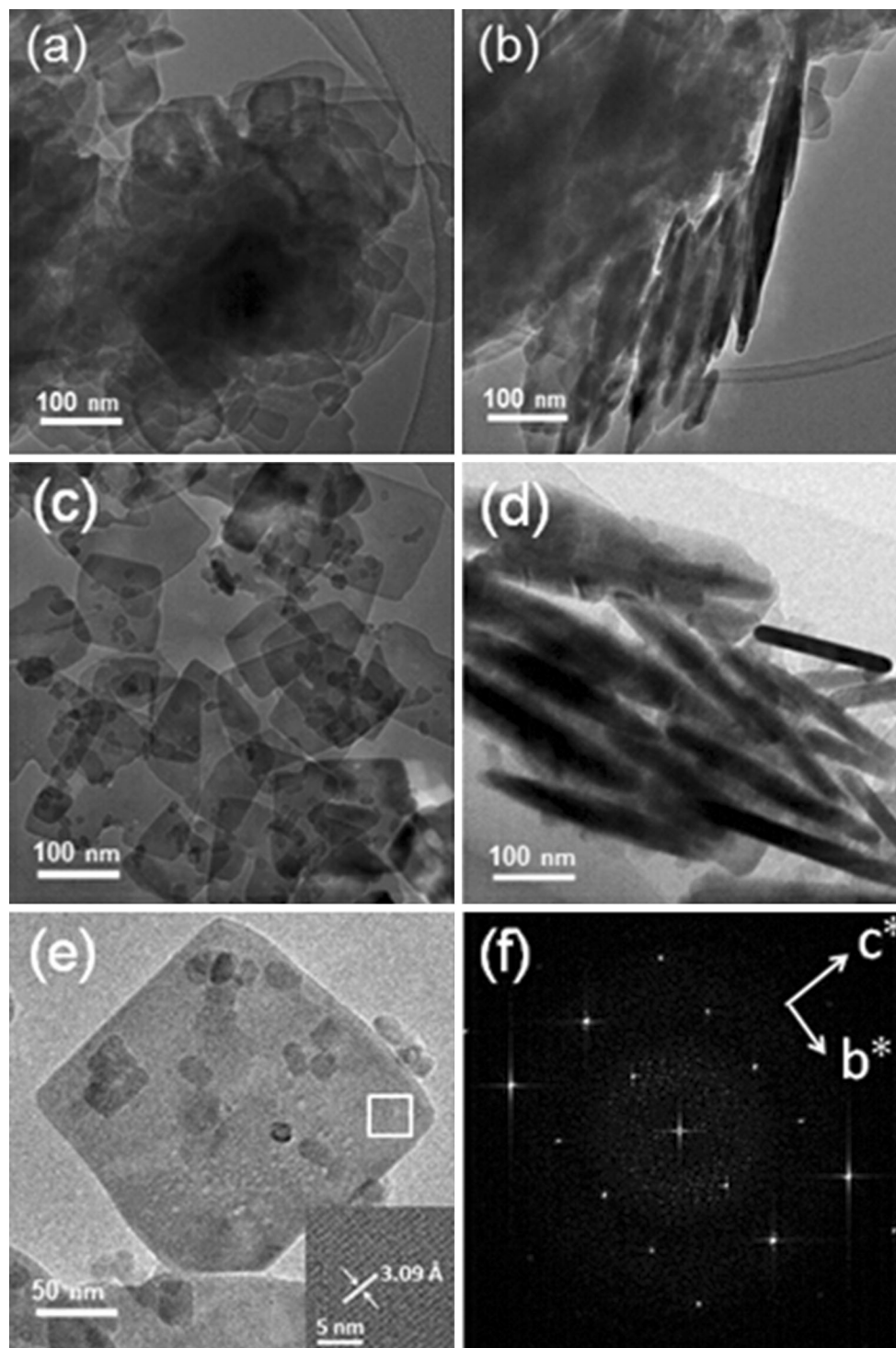


Figure 3 TEM images of **a, b** LMP-N and **c–e** LMP-S; the *inset* in **e** and pattern **f** are the HRTEM image and the FFT pattern of the marked area in image **e**.

alternate nanosheet/nanoparticle sandwich morphology was obtained. As shown in Fig. 2c, d, the nanosheets are with the length and width in the range of 100–200 nm and thickness of about 20 nm,

which is similar to that of LMP-N. The diameters of spheroidal nanoparticles range from 10 to 25 nm, much smaller than that of nanosheets. However, these spheroidal nanoparticles are large enough to

attach themselves onto the surfaces of each nanosheet and prevent them from agglomeration and overlapping, which is supposed to be effective for the sufficient diffusion of electrolyte and helpful to decrease the insertion/extraction distance of lithium ion during the charging and discharging processes as the cathode materials.

Figure 3 shows the TEM images of LMP-N and LMP-S as well as the HRTEM image and the fast Fourier transform (FFT) pattern of LMP-S. Obviously severe agglomeration happens for LMP-N and the LiMnPO_4 nanosheets aggregate densely without effective diffusion channel between them (Fig. 3a, b). From Fig. 3c and d, preferable dispersibility can be observed for LMP-S with the alternate nanosheet/nanoparticle sandwich morphology, in which we can see gaps equal to the size of LiMnPO_4 nanoparticle between each two nanosheets. It suggests that nanoparticles prevent the nanosheets from overlapping and agglomeration. At the same time, as shown in Fig. 3c, the LiMnPO_4 nanoparticles are evenly distributed on the surfaces of LiMnPO_4 nanosheets without any self-aggregation, which results in the feasible electrolyte transfer path. The HRTEM image inserted in Fig. 3e shows the interplanar spacing of 3.09 Å corresponding to the (020) lattice plane of LiMnPO_4 (JCPDS card No. 74-0375). The FFT pattern as shown in Fig. 3f demonstrates that the largest exposed crystalline faces of the LiMnPO_4 nanosheets for LMP-S are the (100) planes, which is in accordance with the above XRD result.

Figure 4 represents the N_2 adsorption–desorption isotherms and the BJH pore size distribution of LMP-N and LMP-S. According to the Brunauer–Emmett–Teller (BET) method, the surface area of LMP-S is

estimated to be $61 \text{ m}^2 \text{ g}^{-1}$, while the surface area of LMP-N is estimated to be $33 \text{ m}^2 \text{ g}^{-1}$, which can obviously supply more electrolyte contact sites and make the insertion/extraction of lithium ion easier during charging and discharging. The increase of the BET surface area of LMP-S compared to that of LMP-N could be attributed to two reasons. One is the existence of spheroidal nanoparticles with diameter of ca. 20 nm. Another more important reason is that the spheroidal nanoparticles prevent the nanosheets from overlapping and agglomeration, and thus can make the surfaces of nanosheets to be exposed to a great extent. The hysteresis loops in Fig. 4 arise at the higher p/p_0 , indicating the existence of mesopores within the two samples. The stronger hysteresis for LMP-S means a greater degree of capillary condensation or in other words, much more interconnected mesopores than LMP-N. The pore volume of LMP-S has been measured to be $0.41 \text{ cm}^3 \text{ g}^{-1}$, much larger than that of LMP-N ($0.20 \text{ cm}^3 \text{ g}^{-1}$), which confirms the above observations from the SEM and TEM images.

The inset in Fig. 4 shows the pore size distribution results of LMP-N and LMP-S. We can see that the pore size distribution of LMP-N is wider than that of LMP-S with the average pore size of ca. 20 nm, which comes from the aggregation of nanosheets in LMP-N. For LMP-S, the pore size peak appears to be about 10–30 nm centered at ca. 18 nm, which is similar to the size (10–25 nm) of spheroidal nanoparticles existing in LMP-S. Is this just a coincidence? We would like to find out the reason behind it. As is well known, Kelvin equation is one of the basic theories for N_2 adsorption–desorption test [45]. If the material pores are cylinder shaped, the concave liquid curved surface formed by N_2 through capillary condensation is that of spherical curved surface (shown in Fig. 5a) and according to the Kelvin equation, the relative pressure p/p_0 and the spherical radius r have the following relationship (Eq. 1):

$$\ln \frac{p}{p_0} = \frac{2M\gamma}{\rho RT} \cdot \frac{1}{r} \quad (1)$$

where M is the molar mass of N_2 , γ is the surface tension, ρ is the density of liquid N_2 , R is the gas constant, T is the absolute temperature, p/p_0 is the relative pressure, and r is the spherical curved surface radius. If the material pores are constructed by twin-slab, the concave liquid curved surface formed by N_2 through capillary condensation is no longer the

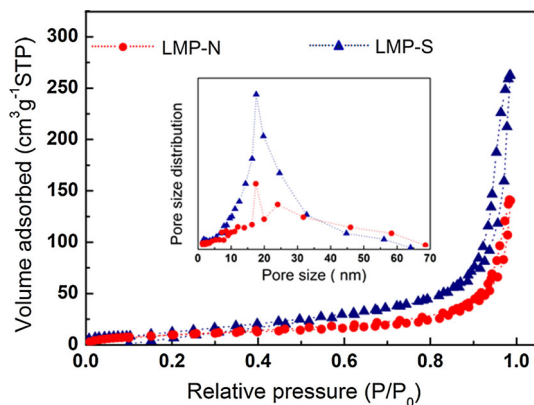


Figure 4 N_2 adsorption and desorption isotherms and BJH pore size distributions (*inset*) of LMP-N and LMP-S.

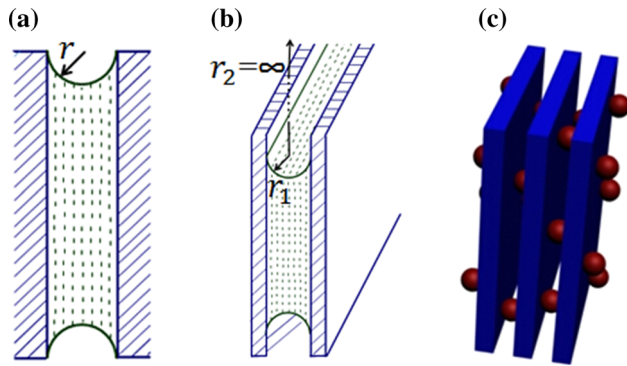


Figure 5 Schematic diagrams of **a** capillary condensation in cylinder model, **b** capillary condensation in twin-slab model, and **c** sandwich nanostructure constructed by nanosheets and nanoparticles.

spherical curved surface but an aspherical curved surface (see Fig. 5b), and the relative pressure p/p_0 and the two principal radii of curvature, (r_1 and r_2), have the following relationship (Eq. (2)) [46]:

$$\ln \frac{p}{p_0} = \frac{2M\gamma}{\rho RT} \cdot \left(\frac{1}{2r_1} + \frac{1}{2r_2} \right) \quad (2)$$

where M is the molar mass of N_2 , γ is the surface tension, ρ is the density of liquid N_2 , R is the gas constant, T is the absolute temperature, p/p_0 is the relative pressure, and r_1 and r_2 are the two principal radii of curvature. BJH (Barrett–Joyner–Halenda) method is the application of Kelvin equation in cylinder model (see Fig. 5a), which means that the calculation process is based on Eq. 1. Consequently, for every different kind of pores, the pore size is characterized to be equal to r as per calculation using the spherical curved surface. However, the length and width of nanosheets in LMP-S (100–200 nm) are relatively large (see Figs. 2, 3). It is apparently more suitable to use twin-slab model (Fig. 5b) to calculate the pore sizes for the as-synthesized LMP-S samples. As shown in Fig. 5b, when the capillary condensation happens between two slabs, one of the two principal radii of curvature tends to infinity ($r_2 = \infty$). Accordingly, the calculated pore size equals to $2r_1$. At the same time, from the pore size distribution results, and the SEM and TEM images, it is obvious that the pore size distribution of LMP-S (18 nm) is equivalent to the size of nanoparticles (10–25 nm). Hence, the size of nanoparticles in LMP-S is equal to $2r_1$, which is obviously the distance between the two slabs. As a result, we can conclude that the distance of two nanosheets in LMP-S is equal to the diameter of

nanoparticles in LMP-S. In other words, most of the micromorphology of LMP-S is of the alternate nanosheet/nanoparticle sandwich nanostructure as shown in Fig. 5c, which is in accordance with the SEM and TEM images.

The above XRD, SEM, TEM, and N_2 adsorption measurements reveal that the main differences between LMP-N and LMP-S are their morphology, dispersibility, and porosity. The nanosheets in LMP-N stack all together with dense surface and rare pores. As an apparent contrast, the existence of spheroidal $LiMnPO_4$ nanoparticles on the surface of each nanosheet in LMP-S facilitates the formation of an ultradispersed sandwich nanostructure, which prevents the nanosheets from overlapping and agglomeration, and thus results in the high surface area and abundant mesopores channel for LMP-S.

After the synthesis of $LiMnPO_4/C$ process, the carbon-coating morphology of both $LiMnPO_4$ samples can be shown by the contrast TEM images in Fig. 6. Obviously, due to the presence of severe agglomeration phenomenon for pure nanosheets sample, the carbon-coating morphology of LMP-N/C is also aggregate and nonuniform in nature (shown in Fig. 6a, c). The pyrolytic carbon coats onto the surfaces of the heavily agglomerated bulks, in which the nanosheets cannot be distinguished any longer. For the LMP-S/C sample, due to the sandwich nanostructure, the dispersibility is maintained well. The glucose pyrolyzed homogeneously on the surfaces of the sandwich nanostructured $LiMnPO_4$. Both $LiMnPO_4$ nanosheets and nanoparticles are very well dispersed in the carbon matrix with the carbon-coating thickness of ca. 2–4 nm as shown in Fig. 6b, d. The fully exposed crystal surfaces and abundant pores of the sandwich nanostructured $LiMnPO_4$ sample (as shown in Fig. 4) lead to not only the subsequent uniform carbon-coating but also to make more effective contact between the active material and the electrolyte, which will result in fast and homogeneous lithium-ion insertion and extraction. Both the LMP-N/C and LMP-S/C samples were synthesized with the addition of the as-synthesized $LiMnPO_4$ into the glucose solution with a same molar ratio of 2:1 for $LiMnPO_4$ and glucose. However, the carbon contents (wt%) were estimated to be ca. 10 and 16 wt% for LMP-N/C and LMP-S/C, respectively, by TGA as shown in Fig. 7. The extra carbon (6 wt%) in LMP-S/C could be ascribed to two reasons. One reason is that pyrolyzation of residual oleic

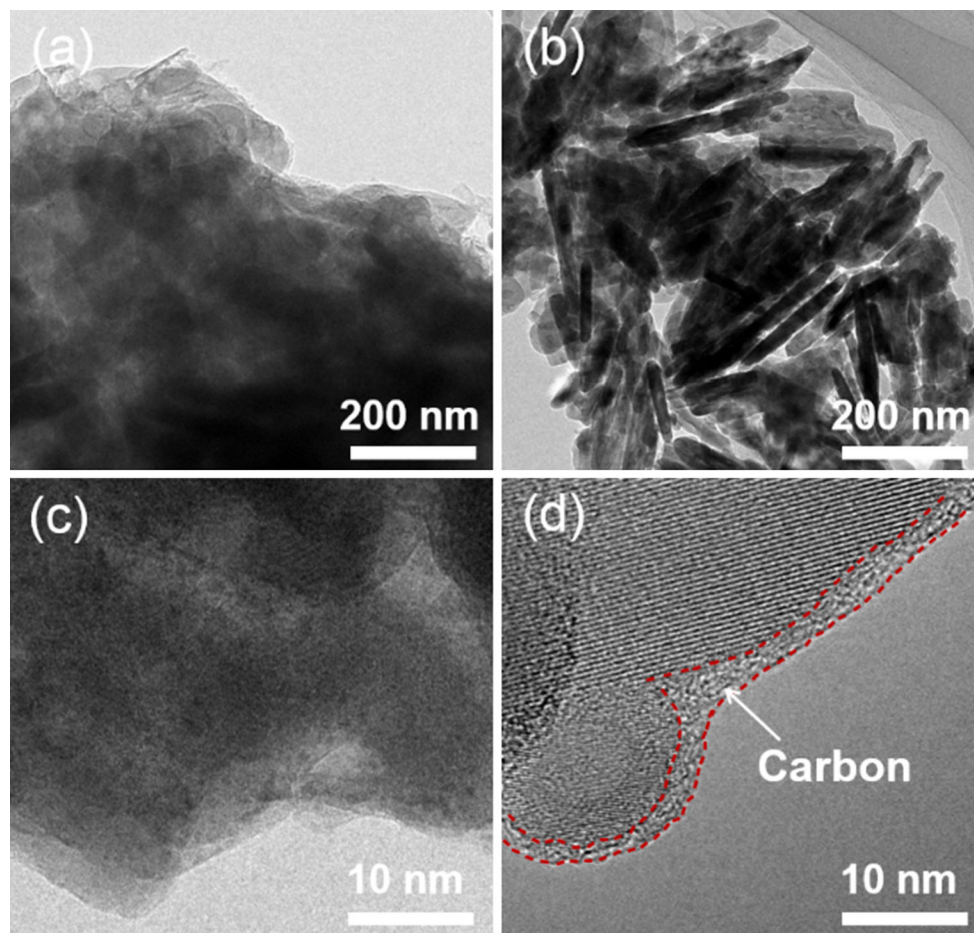


Figure 6 TEM images of the carbon-coated LiMnPO_4 samples: **a, c** LMP-N/C and **b, d** LMP-S/C.

acid chelating on the particle surfaces of the LMP-S sample contributes to the extra carbon during carbon-coating process. Another more important reason is that owing to the good dispersibility of LMP-S which facilitates coating each crystal with pyrolytic carbon instead of just coating surfaces of the agglomerated particles for LMP-N. In brief, the excellent alternate sandwich nanostructured morphology of LMP-S could be beneficial to reduce the polarization and improve the electrochemical performances for LMP-S/C.

In this study, based on the contrast synthesis of LMP-N and LMP-S (see Fig. 8), we can see that oleic acid plays an important role in the formation of the novel alternate sandwich nanostructure for LMP-S. Solvothermal pathway, compared with other synthesis methods such as solid-state preparation, may allow control of the materials morphology by tuning the synthesis parameters [47, 48]. Based on the above characterization data, we can see that

nanosheet/nanoparticle sandwich nanostructure with good dispersibility could be obtained by the oleic acid-assisted synthesis method herein for LMP-S. It is known that oleic acid with carboxylic acid group can chelate some metal ions and adsorb onto certain crystal planes as a surfactant or capping agent to provide coordination function or steric hindrance and has been widely advocated in the chemical synthesis of nanoscale materials [49, 50]. In this work, the part complexation of proper amount of oleic acid leads to the nucleation and subsequent growth of some LiMnPO_4 phase in a controlled manner, resulting in the existing of some spheroidal nanoparticles in LMP-S (Fig. 8) [51]. For nanostructured design, this method is simple, effective, and of low cost. In the process, a fraction of nucleation centers was wrapped up forming microballoons in which the nucleation center was bound and lost the chance to develop into nanoplate but instead into the pony-sized LiMnPO_4 spheroidal particle. Duo the

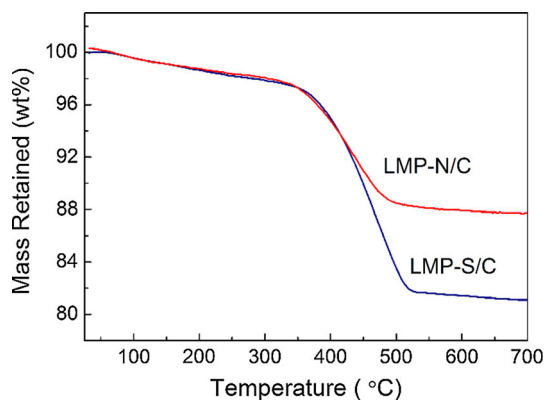


Figure 7 TGA curves of LMP-N/C and LMP-S/C.

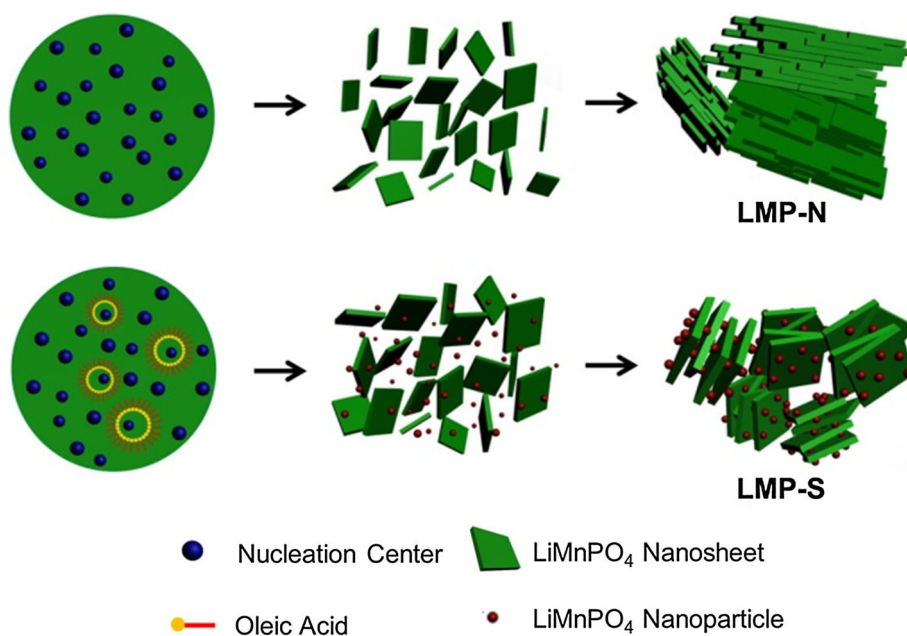
high specific surface area, LiMnPO_4 spheroidal particles would not exist alone and adhere onto the surface of LiMnPO_4 nanosheet resulting in the self-assembly of sandwich nanostructure. This novel alternate sandwich nanostructure avoids the unnecessary agglomerations of nanosheets, improves the dispersibility, and increases the surface areas, and pore volumes of LiMnPO_4 , which have been proven by the above SEM, TEM, and N_2 adsorption characterizations and should be advantageous for the improvement of their electrochemical properties.

In order to clarify the differences in the electrochemical performances between LMP-N and LMP-S, the cyclic voltammogram (CV) measurements of both the carbon-coated LiMnPO_4 samples (LMP-N/C,

LMP-S/C) were carried out in the potential range of 2.0–4.5 V at a scan rate of 0.1 mV s^{-1} (Fig. 9). A reduction peak at approximately 3.9 V and an oxidation peak at approximately 4.4 V appeared for both samples and could be attributed to the $\text{Mn}^{2+}/\text{Mn}^{3+}$ redox couple, which is comparable to that of the reported LiMnPO_4/C cathodes [19, 52]. Compared with the LMP-N/C sample, LMP-S/C shows an increased current at both the anodic peak and the cathodic peak. The increased intensity of both peaks for LMP-S/C could be attributed to the kinetic improvements, resulting from the enhanced conductivity [29, 53], which is supposed to speed up the mobility of lithium ion and lead to a higher special capacity during charging and discharging processes.

Based on the above discussed morphology, structure, and CV properties, the LMP-S/C cathode is expected to provide an enhanced performance in lithium-ion batteries. To confirm this prevision, we compared its electrochemical performance to that of the LMP-N/C cathode. Figure 10a, b shows the charge and discharge curves of both carbon-coated LiMnPO_4 samples at various charge/discharge rates ranging from 0.05 to 5 C in the voltage range between 2.0 and 4.5 V. As shown in Fig. 10a, b, the charge capacity is nearly 200 mAh g^{-1} in the first cycle for both LMP-N/C and LMP-S/C, although the theoretical specific capacity of LiMnPO_4 is 171 mAh g^{-1} . It is because SEI (Solid electrolyte interphase) film is formed. SEI film results from the reaction between

Figure 8 Schematic diagram of synthesis reaction mechanism.



the active material and electrolyte in the first cycle, which will contribute to the capacity of batteries [2, 36]. The voltage profile of LMP-S/C clearly shows a much flatter plateau around 4.0 V vs. Li/Li⁺ compared to that of LMP-N/C. The discharge special capacities generally decreased as the rate increased for the both LiMnPO₄ cathodes. The first discharge capacity of LMP-S/C at 0.05 C rate is 164.9 mAh g⁻¹, and at various rates, the discharge capacities are 159.6 mAh g⁻¹ at 0.1 C, 142.5 mAh g⁻¹ at 0.2 C, 122.0 mAh g⁻¹ at 0.5 C, 107.3 mAh g⁻¹ at 1 C, 93.7 mAh g⁻¹ at 2 C, and 77.6 mAh g⁻¹ at 5 C, respectively. Similarly, the discharge capacities at

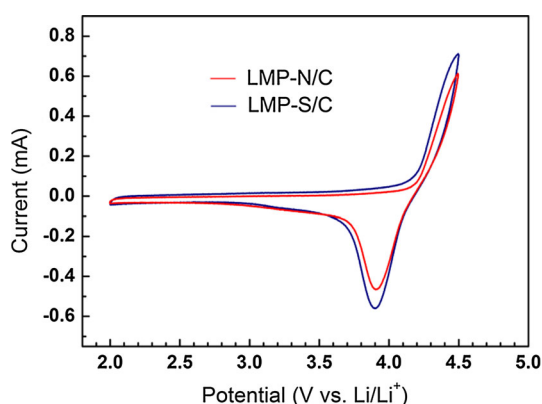
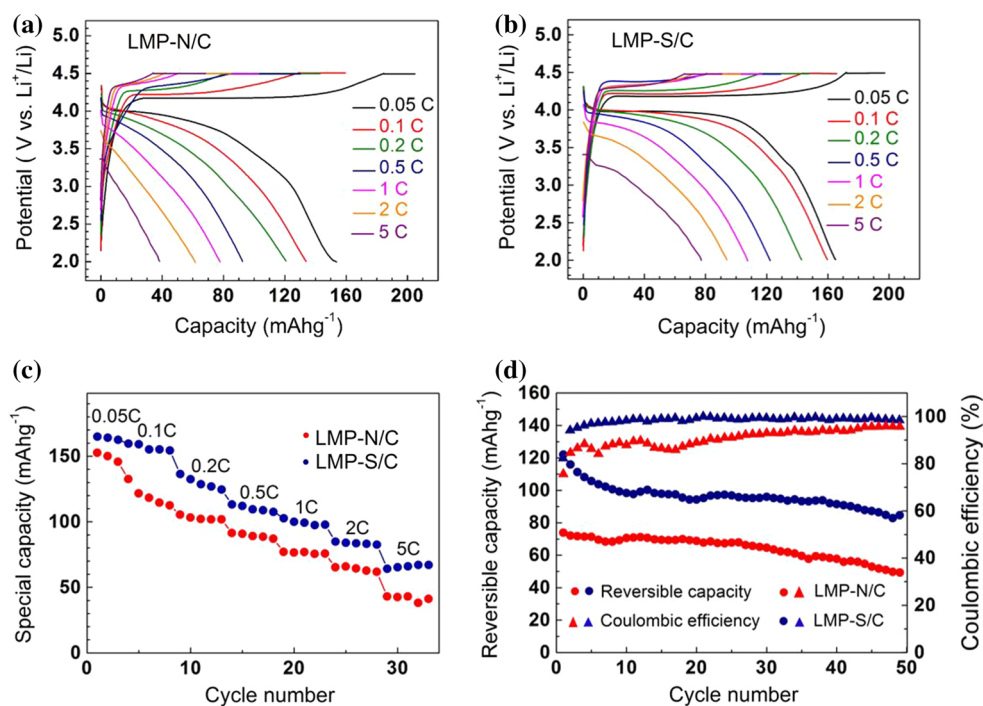


Figure 9 Cyclic voltammograms of LMP-N/C and LMP-S/C. The scan rate was 0.1 mV s⁻¹.

various rates for LMP-N/C are 153.3 mAh g⁻¹ at 0.05 C, 133.5 mAh g⁻¹ at 0.1 C, 120.3 mAh g⁻¹ at 0.2 C, 92.4 mAh g⁻¹ at 0.5 C, 77.8 mAh g⁻¹ at 1 C, 61.7 mAh g⁻¹ at 2 C, and 38.9 mAh g⁻¹ at 5 C, respectively. Although the CV curves shown in Fig. 9 display heavy polarization of the electrodes and the plateaus of the charge–discharge curves are not very long, high special capacity could be still be reached at the lower rate especially for sample LMP-S/C. Besides, the sample LMP-S/C shows smaller polarization and more persistent plateau at all rates than the LMP-N/C due to the sandwich nanostructure morphology. We notice that the discharge special capacities of LMP-S/C present a smaller recession than that of LMP-N/C as the discharge rates increase. When the discharge rate increased to 5 C, the discharge capacity delivered by LMP-S/C was nearly twofolds higher than that of LMP-N/C electrode with disparity being as large as 38.7 mAh g⁻¹. The smaller deterioration of discharge capacity for LMP-S/C could be ascribed to the favorable dispersibility, large surface area, and abundant mesopores, which provide for more efficient contact between the active material and electrolyte and better lithium-ion insertion and extraction [6, 54]. Figure 10c compares the rate capabilities of LMP-S/C and LMP-N/C. Apparently, LMP-S/C delivers the much higher capacities at all rates than LMP-N/C does. More notably, there is a sharp decline (as high as 26 %) of

Figure 10 Voltage profiles of LMP-N/C (a) and LMP-S/C (b) at various charge/discharge rates; Rate capabilities of LMP-N/C and LMP-S/C at different discharge rates (c); Cycling performances and coulombic efficiencies (d) of LMP-N/C and LMP-S/C at a discharge rate of 0.5 C.



discharge capacity for LMP-N/C even at the initial rates from 0.05 C to 0.1 C, while low decay (6 %) of capacity is found for LMP-S/C during the first 8 cycles. We can also see a quite large disparity of capacities between LMP-S/C and LMP-N/C from the cycle performance as shown in Fig. 10d. After a total of 50 cycles, LMP-S/C shows an outstanding 1.7 times higher special capacity, which is also 35.5 mAh g⁻¹ larger than that of LMP-N/C. In addition, LMP-S/C shows higher coulombic efficiency than LMP-N/C all over the 50 cycles. All the above go to prove the importance of this ultradispersed sandwich nanostructure for improving the electrochemical properties of carbon-coated LiMnPO₄ as the cathode materials. The LMP-S/C electrode makes progress in special capacities compared with the LMP-N/C electrode, but we can find that cycle performance of the LMP-S/C sample is not very good. This could be ascribed to the mechanical degradation, such as lattice damage in active materials [55], which imposes a significant bearing on LIB life and performance decay in terms of capacity. Mechanical degradation mainly caused by the solid-state diffusion of lithium ions induced stress in the active particles [56, 57]. Figure S1a, b shows the TEM images of the LMP-S/C sample scraped from the electrodes after being charged and discharged for 50 cycles. We can clearly see a certain degree of lattice damage of the LMP-S/C sample.

In order to evidence that the reduction of polarization of the electrodes during charge and discharge processes is a favorable benefit resulting from the sandwich nanostructure morphology of LMP-S, but not from the addition of extra carbon, we also synthesized the LMP-N/C-16 % the carbon content of which is ca. 16 wt% by increasing the amount of glucose (LMP-N:glucose = 1.16:1 in molar ratio) in the carbon-coating process. Fig. S2 shows the Cyclic voltammograms of LMP-N/C-16 % and LMP-N/C. For both LMP-N/C-16 % and LMP-N/C, the reduction and oxidation peaks appeared at the same positions (3.9 and 4.4 V, respectively) at the same values of current (−0.5 and 0.6 mA, respectively). We can thus draw a conclusion that the electrochemical performances of LMP-N/C-16 % and LMP-N/C are nearly the same, which evidences that the reduction of polarization of the electrodes during charge and discharge processes is a favorable benefit from the sandwich nanostructure morphology of LMP-S, but not from extra carbon adding.

To further clarify the difference in the electrochemical activities between LMP-N/C and LMP-S/C, the electrochemical impedance spectra (EIS) tests of coin cells were carried out for both samples. As shown in Fig. 11, it is apparent that the spectra of both LMP-N/C and LMP-S/C conclude a semicircle at high-frequency region and a straight line at low-frequency region. As is well known, the dimension of the semicircle reflects the overall cell charge-transfer resistance [10, 58]. Electron transport over the surface of the active material is a main component of the overall charge-transfer resistance. It is obvious that a much smaller semicircle is observed for LMP-S/C, which indicates the accelerated electron transport over surface of the LMP-S/C sample due to the uniform carbon layer resulting from the sandwich nanostructure [59]. The plots are fitted by the equivalent circuit as shown in the inset of Fig. 11, where R_e represents the electrolyte resistance, and R_{ct} represents the charge-transfer resistances. Besides, Z_w is the Warburg impedance revealed at the low frequencies which is related to the Li ions diffusion in the bulk material. These two spectra have been used to calculate the Li ions diffusion coefficients (D_{EIS}) of LMP-N/C and LMP-S/C according to the Warburg equation [60]:

$$D_{EIS} = \frac{1}{2\omega_f} \left(\frac{RT}{z^2 F^2 C A R_w} \right)^2 \quad (3)$$

where R is the gas constant (8.314 J K⁻¹ mol⁻¹), T is the temperature (K), ω_f is the final frequency of the measurement (0.1 Hz), $z = 1$ is the number of

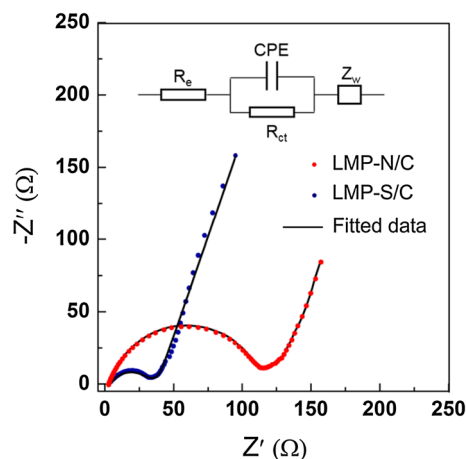


Figure 11 Electrochemical impedance spectra of LMP-N/C and LMP-S/C within the frequency range of 100 kHz to 0.1 Hz and the corresponding fitting using equivalent circuit (*inset*).

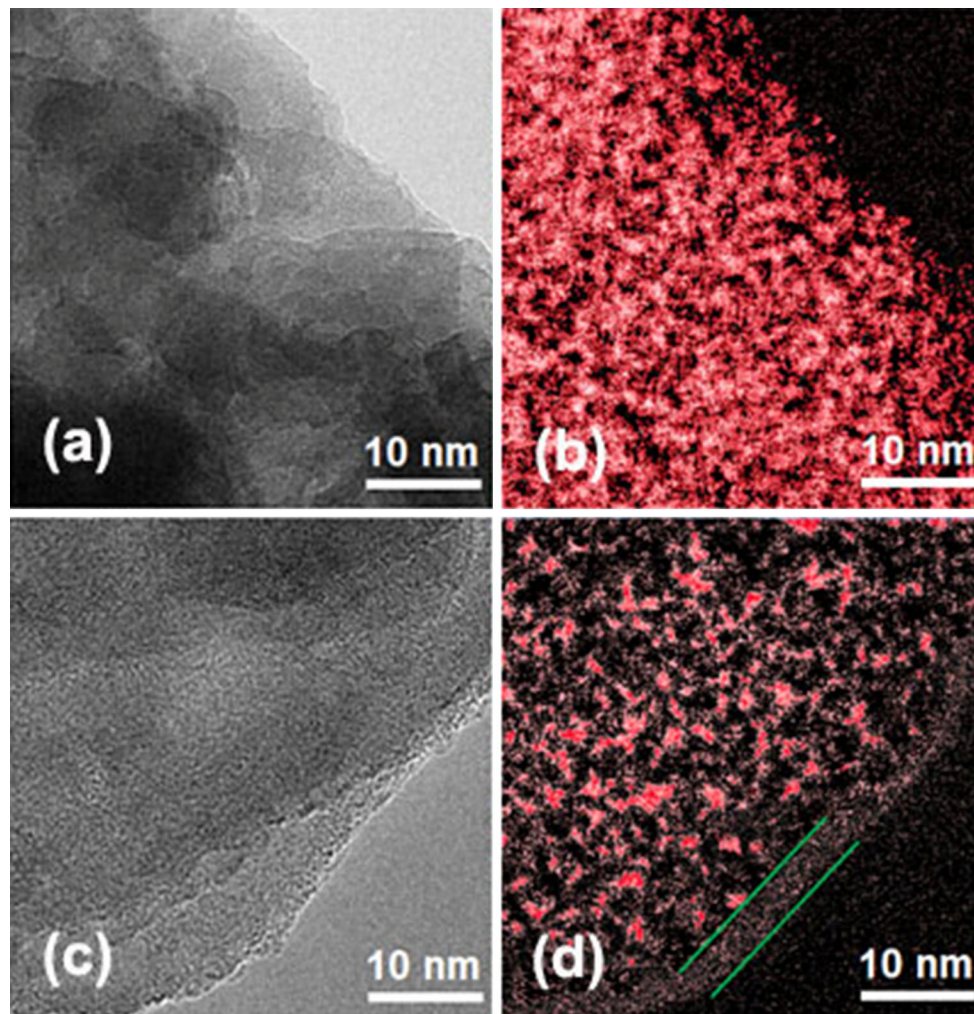


Figure 12 TEM images (a, c) and corresponding Li-EELS mapping images (b, d) of LMP-N/C (a, b) and LMP-S/C (c, d). These electrodes were charged in CC–CV mode at 0.5 C.

exchanged electrons, F is the Faraday constant ($96,485 \text{ C mol}^{-1}$), C is the Li^+ concentration within the olivine lattice ($0.022 \text{ mol cm}^{-3}$), A is the electrode geometric area (1.32 cm^2), and R_w is the Warburg resistance. R_w has been determined by nonlinear least-squares (NNLS) analysis. The calculated Li ions' diffusion coefficients for LMP-N/C and LMP-S/N are 7.9×10^{-14} and $9.98 \times 10^{-13} \text{ cm}^2 \text{ S}^{-1}$, respectively. The value of D_{EIS} for LMP-S/C is an order magnitude bigger than that for LMP-N/C. LMP-S/C shows much better Li-ion diffusion rate than LMP-S/C, which could be ascribed to uniform post carbon coating and the more effective contact between electrolyte and active material for LMP-S/C [61, 62]. In addition, Table S1 reports the R_e and R_{ct} values calculated by NNLS analysis. Again, LMP-S/C shows the much lower R_{ct} value (27.7Ω) than LMP-N/C

(103.2Ω). The abundant mesoporous in the sandwich nanostructure is excellent channel for the exchange of electrons between carbon-coated LiMnPO_4 and the electrolyte.

To better understand the mechanisms of alternate sandwich nanostructure for the improved electrochemical property of LMP-S/C, TEM images and the corresponding Li-EELS mapping images of charged LMP-N/C and LMP-S/C electrodes were carried out and are shown in Fig. 12. Both samples were scraped from the electrodes after being charged in CC–CV mode at 0.5 C. From the TEM image of LMP-N/C shown in Fig. 12a, we can see that severe agglomeration happens, and the pure nanosheet morphology cannot be seen clearly. In contrast, the dispersive nanosheet outline of LMP-S/C is still unambiguous even after the carbon-coating and charging processes

as shown in Fig. 12c. Figure 12d shows the Li-EELS mapping image of LMP-S/C. It is clearly visible that lithium element distributes rather evenly along the vacancies in both the center and the edge of the nanosheets, which highlights the advantage of sandwich nanostructured LiMnPO_4 as cathode material for lithium-ion battery. Besides, a conspicuous and homogeneous carbon layer (2–4 nm in thickness) covering on the LiMnPO_4 surface for LMP-S/C can be observed. In contrast, a much higher density of lithium element can be seen in Fig. 12b for LMP-N/C cathode, and no obvious carbon layer can be detected. The much lower density of lithium on the Li-EELS mapping for charged LMP-S/C is associated with the above-mentioned improved electrochemical performance. The enhanced lithium storage results could be attributed to the highly dispersed and sandwich nanostructure for LMP-S/C, which facilitates the electrolyte mass diffusion and lithium-ion transport, and ensures highly homogeneous carbon coating and decreased polarization [19, 63]. Hence, fast ion and electron conductions were attained, resulting in the enhanced electrochemical performance for the sandwich nanostructured LiMnPO_4 .

Conclusions

Sandwich nanostructured LiMnPO_4/C cathode material is prepared with the addition of proper amount of oleic acid during the solvothermal synthesis. The electrode has an alternate nanosheet/nanoparticle morphology by the partial steric hindrance effect of oleic acid. This sandwich nanostructured LiMnPO_4/C delivers a discharge capacity of 164.9 mAh g^{-1} at 0.05 C charge–discharge rate and of ca. 85.6 mAh g^{-1} at 0.5 C after 50 cycles. This outstanding performance can be ascribed to the novel alternate sandwich nanostructure of LiMnPO_4 , which has better dispersibility, larger surface area, and boarder mesoporous distribution. These microstructures are favorable to enhancing the electrolyte contact, reduce the lithium-ion diffusion length, promote the uniformity of post carbon coating, and finally obtain the enhanced electrode performances. The construction of sandwich nanostructured cathode material which simultaneously satisfies fast lithium-ion diffusion and high electrical conductivity can be a potential strategy to

improve the electrochemical performances of electrode materials.

Acknowledgements

This work was supported by the Project Nos. 51472179 and 51572192 supported by the National Natural Science Foundation of China; the Fund for the Doctoral Program of Higher Education, Ministry of Education of China (20120032120017); and the General Program of Municipal Natural Science Foundation of Tianjin (13JCYBJC16900, 13JCQJNC08200).

Compliance with ethical standards

Conflict of interest The authors declare that they have no conflict of interest.

Electronic supplementary material: The online version of this article (doi:10.1007/s10853-016-0417-3) contains supplementary material, which is available to authorized users.

References

- [1] Bruce PG, Scrosati B, Tarascon JM (2008) Nanomaterials for rechargeable lithium batteries. *Angew Chem Int Ed* 47:2930–2946
- [2] Cheng FY, Tao ZL, Liang J (2008) Chen, J. Template-directed materials for rechargeable lithium–ion batteries. *Chem Mater* 20:667–681
- [3] Liu Q, Li ZF, Liu Y, Zhang H, Ren Y, Sun CL, Lu W, Zhou Y, Stanciu L, Stach EA, Xie J (2015) Graphene-modified nanostructured vanadium pentoxide hybrids with extraordinary electrochemical performance for Li-ion batteries. *Nat Commun* 6:127
- [4] Padhi AK, Nanjundaswamy KS, Goodenough JB (1997) Phospho-olivines as positive-electrode materials for rechargeable lithium batteries. *J Electrochem Soc* 144: 1188–1194
- [5] Chung SY, Bloking JT, Chiang YM (2002) On the electronic conductivity of phospho-olivines as lithium storage electrodes. *Nat Mater* 1:702–703
- [6] Yoo H, Jo M, Jin BS, Kim HS, Cho J (2011) Flexible morphology design of 3D-macroporous LiMnPO_4 cathode materials for Li secondary batteries: ball to flake. *Adv Energy Mater* 1:347–351

- [7] Nagaraju DH, Kuezman M, Suresh GS (2015) LiFePO₄ wrapped reduced graphene oxide for high performance Li-ion battery electrode. *J Mater Sci* 50:4244–4249. doi:10.1007/s10853-015-8976-2
- [8] Qiu YJ, Geng YH, Yu J, Zuo XB (2014) High-capacity cathode for lithium-ion battery from LiFePO₄/(C + Fe₂P) composite nanofibers by electrospinning. *J Mater Sci* 49:504–509. doi:10.1007/s10853-013-7727-5
- [9] Rousse G (2003) Magnetic Structures of the triphylite LiFePO₄ and of its delithiated form FePO₄. *Chem Mater* 15:4082–4090
- [10] Oh SM, Oh SW, Yoon CS, Scrosati B, Amine K, Sun YK (2010) High-performance Carbon-LiMnPO₄ nanocomposite cathode for lithium batteries. *Adv Funct Mater* 20:3260–3265
- [11] Ma GF, Peng H, Mu JJ, Huang HH, Zhou XZ, Lei ZQ (2013) In situ intercalative polymerization of pyrrole in graphene analogue of MoS₂ as advanced electrode material in supercapacitor. *J Power Sources* 229:72–78
- [12] Bramnik NN, Nikolowski K, Trots DM, Ehrenberg H (2008) Thermal stability of LiCoPO₄ cathodes. *Electrochem Solid State* 11:A89–A93
- [13] Markevich E, Sharabi R, Gottlieb H, Borgel V, Fridman K, Salitra G, Aurbach D, Semrau G, Schmidt MA, Schall N, Bruening C (2012) Reasons for capacity fading of LiCoPO₄ cathodes in LiPF₆ containing electrolyte solutions. *Electrochem Commun* 15:22–25
- [14] Nakamura T, Miwa Y, Tabuchi M, Yamada Y (2006) Structural and surface modifications of LiFePO₄ olivine particles and their electrochemical properties. *J Electrochem Soc* 153:A1108–A1114
- [15] Yuan LX, Wang ZH, Zhang WX, Hu XL, Chen JT, Huang YH, Goodenough JB (2011) Development and challenges of LiFePO₄ cathode material for lithium-ion batteries. *Energy Environ Sci* 4:269–284
- [16] Martha SK, Markovsky B, Grinblat J, Gofer Y, Haik O, Zinigrad E, Aurbach D, Drezen T, Wang D, Deghenghi G, Exnar I (2009) LiMnPO₄ as an advanced cathode material for rechargeable lithium batteries. *J Electrochem Soc* 156:A541–A552
- [17] Kim J, Kim H, Park KY, Park YU, Lee S, Kwon HS, Yoo HI, Kang K (2014) Alluaudite LiMnPO₄: a new Mn-based positive electrode for Li rechargeable batteries. *J Mater Chem A* 2:8632–8636
- [18] Herle PS, Ellis B, Coombs N, Nazar LF (2004) Nano-network electronic conduction in Iron and nickel olivine phosphates. *Nat Mater* 3:147–152
- [19] Cao Y, Duan J, Hu G, Jiang F, Peng Z, Du K, Guo H (2013) Synthesis and electrochemical performance of nanostructured LiMnPO₄/C composites as lithium-ion battery cathode by a precipitation technique. *Electrochim Acta* 98:183–189
- [20] Fisher CAJ, Prieto VMH, Islam MS (2008) Lithium Battery Materials LiMPO₄ (M = Mn, Fe Co, and Ni): Insights into defect association, transport mechanisms, and doping behavior. *Chem Mater* 20:5907–5915
- [21] Tang P, Holzwarth NAW (2003) Electronic structure of FePO₄, LiFePO₄, and related materials. *Phys Rev B* 68:165107
- [22] Meethong N, Kao YH, Tang M, Huang HY, Carter WC, Chiang YM (2008) Electrochemically induced phase transformation in nanoscale olivines Li_{1-x}MPO₄ (M = Fe, Mn). *Chem Mater* 20:6189–6198
- [23] Arico AS, Bruce P, Scrosati B, Tarascon JM, Schalkwijk WV (2005) Nanostructured materials for advanced energy conversion and storage devices. *Nat Mater* 4:366–377
- [24] Kang B, Ceder G (2009) Battery materials for ultrafast charging and discharging. *Nature* 458:190–193
- [25] Kwon NH, Drezen T, Exnar I, Teerlinck I, Isono M, Graetzel M (2006) Enhanced electrochemical performance of mesoparticulate LiMnPO₄ for lithium ion batteries. *Electrochem Solid-State Lett* 9:A277–A280
- [26] Wang YR, Yang YF, Yang YB, Shao HX (2010) Enhanced electrochemical performance of unique morphological LiMnPO₄/C cathode material prepared by solvothermal method. *Solid State Commun* 150:81–85
- [27] Barpanda P, Djellab K, Recham N, Armand M, Tarascon JM (2011) Direct and modified ionothermal synthesis of LiMnPO₄ with tunable morphology for rechargeable Li-ion batteries. *J Mater Chem* 21:10143–10152
- [28] Wang DY, Buqa H, Crouzet M, Deghenghi G, Drezen T, Exnar I, Kwon NH, Miners JH, Poletto L, Graetzel M (2009) High-performance, nano-structured LiMnPO₄ synthesized via a polyol method. *J Power Sources* 189:624–628
- [29] Bakenov Z, Taniguchi I (2010) Physical and electrochemical properties of LiMnPO₄/C composite cathode prepared with different conductive carbons. *J Power Sources* 195:7445–7451
- [30] Ni J, Gao L (2011) Effect of copper doping on LiMnPO₄ prepared via hydrothermal route. *J Power Sources* 196:6498–6501
- [31] Ji H, Yang G, Ni H, Roy S, Pinto J, Jiang X (2011) General synthesis and morphology control of LiMnPO₄ nanocrystals via microwave-hydrothermal route. *Electrochim Acta* 56:3093–3100
- [32] Delacourt C, Poizot P, Morcrette M, Tarascon JM, Masquelier C (2004) One-step low-temperature route for the preparation of electrochemically active LiMnPO₄ powders. *Chem Mater* 16:93–99
- [33] Doi T, Yatomi S, Kida T, Okada S, Yamaki JI (2009) Liquid-phase synthesis of uniformly nanosized LiMnPO₄ particles and their electrochemical properties for lithium-ion batteries. *Cryst Growth Des* 9:4990–4992

- [34] Choi D, Wang D, Bae IT, Xiao J, Nie Z, Wang W, Viswanathan VV, Lee YJ, Zhang JG, Graff GL, Yang Z, Liu J (2010) LiMnPO₄ nanoplate grown via solid-state reaction in molten hydrocarbon for Li-ion battery cathode. *Nano Lett* 10:2799–2805
- [35] Arun N, Jain A, Aravindan V, Jayaraman S, Ling WC, Srinivasan MP, Madhavi S (2015) Nanostructured spinel LiNi_{0.5}Mn_{1.5}O₄ as new insertion anode for advanced Li-ion capacitors with high power capability. *Nano Energy* 12:69–75
- [36] Li S, Niu J, Zhao YC, So KP, Wang C, Wang CA, Li J (2015) High-rate aluminium yolk-shell nanoparticle anode for Li-ion battery with long cycle life and ultrahigh capacity. *Nat Commun* 6:7872
- [37] Kim Y, Lee JH, Cho S, Kwon Y, In I, Lee J, You NH, Reichmanis E, Ko H, Lee KT, Kwon HK, Ko DH, Yang H, Park B (2014) Additive-free hollow-structured Co₃O₄ nanoparticle Li-ion battery: the origins of irreversible capacity loss. *ACS Nano* 8:6701–6712
- [38] Srinivasan V, Newman J (2004) Discharge model for the lithium iron-phosphate electrode. *J Electrochem Soc* 151:A1517
- [39] Gaberscek M, Dominko R, Jamnik J (2007) Is small particle size more important than carbon coating? an example study on LiFePO₄ cathodes. *J Electrochem Commun* 9:2778–2783
- [40] Rangappa D, Sone K, Zhou Y, Kudo T, Honma I (2011) Size and shape controlled LiMnPO₄ nanocrystals by a supercritical ethanol process and their electrochemical properties. *J Mater Chem* 21:15813–15818
- [41] Cao FF, Guo YG, Zheng SF, Wu XL, Jiang LY, Bi RR, Wan LJ, Maier J (2010) Symbiotic coaxial nanocables: facile synthesis and an efficient and elegant morphological solution to the lithium storage problem. *Chem Mater* 22:1908–1914
- [42] Guo YG, Hu JS, Wan LJ (2008) Nanostructured materials for electrochemical energy conversion and storage devices. *Adv Mater* 20:2878–2887
- [43] Qin Z, Zhou X, Xia Y, Tang C, Liu Z (2012) Morphology controlled synthesis and modification of high-performance LiMnPO₄ cathode materials for Li-ion batteries. *J Mater Chem* 22:21144–21153
- [44] Fang H, Li L, Yang Y, Yan G, Li G (2008) Carbonate anions controlled morphological evolution of LiMnPO₄ crystals. *Chem Commun* 9:1118–1120
- [45] Barrett EP, Joyner LG, Halenda PP (1951) The determination of pore volume and area distributions in porous substances. I. Computations from nitrogen isotherms. *J Am Chem Soc* 73:373–380
- [46] Huang B, Bartholomew CH, Woodfield BF (2014) Improved calculations of pore size distribution for relatively large, irregular slit-shaped mesopore structure. *Micropor Mesopor Mat* 184:112–121
- [47] Lai JP, Niu WX, Luque R, Xu GB (2015) Solvothermal synthesis of metal nanocrystals and their applications. *Nano Today* 10:240–267
- [48] Devaraju MK, Honma I (2012) Hydrothermal and solvothermal process towards development of LiMPO₄ (M = Fe, Mn) nanomaterials for lithium-ion batteries. *Adv Energy Mater* 2:284–297
- [49] Simon P, Bahrig L, Baburin IA, Formanek P, Roeder F, Sickmann J, Hickey SG, Eychmueller A, Lichte H, Kniep R, Rosseeva E (2014) Interconnection of nanoparticles within 2D superlattices of PbS/Oleic acid thin films. *Adv Mater* 26:3042–3049
- [50] Harris RA, Shumbula PM, Walt HVD (2015) Analysis of the interaction of surfactants oleic acid and oleylamine with iron oxide nanoparticles through molecular mechanics modeling. *Langmuir* 31:3934–3943
- [51] Zhang H, Jing L, Zeng J, Hou Y, Li Z, Gao M (2014) Revisiting the coordination chemistry for preparing manganese oxide nanocrystals in the presence of oleylamine and oleic acid. *Nanoscale* 6:5918
- [52] Ramar V, Saravanan K, Gajjela SR, Hariharan S, Balaya P (2013) The effect of synthesis parameters on the lithium storage performance of LiMnPO₄/C. *Electrochim Acta* 105:496–505
- [53] Dinh HC, Mho SI, Kang Y, Yeo IH (2013) Large discharge capacities at high current rates for carbon-coated LiMnPO₄ nanocrystalline cathodes. *J Power Sources* 244:189–195
- [54] Sun YK, Oh SM, Park HK, Scrosati B (2011) Micrometer-sized, nanoporous, high-volumetric-capacity LiMn_{0.85}Fe_{0.15}PO₄ cathode material for rechargeable lithium-ion batteries. *Adv Mater* 23:5050–5054
- [55] Fan CF, Barai P, Mukherjee PP (2014) Diffusion induced damage and impedance response in lithium-ion battery electrodes. *J Electrochem Soc* 161:A2138
- [56] Kalnaus S, Rhodes K, Daniel C (2011) A study of lithium ion intercalation induced fracture of silicon particles used as anode material in Li-ion battery. *J Power Sources* 196:8116
- [57] Hao F, Fang DN (2013) Diffusion-induced stresses of spherical core-shell electrodes in lithium-ion batteries: the effects of the shell and surface/interface stress. *J Electrochem Soc* 160:A595–A600
- [58] Zhang LF, Qu QT, Zhang L, Li J, Zheng HH (2014) Confined synthesis of hierarchical structured LiMnPO₄/C granules by a facile surfactant-assisted solid-state method for high-performance lithium ion batteries. *J Mater Chem A* 2:711–719
- [59] Luo S, Fang HS, Yang B, Yao YC, Ma WH, Dai DY (2013) Improving rate performance of LiMnPO₄ based material by forming electron-conducting iron phosphides. *J Power Sources* 230:267–270

- [60] Lecce DD, Hassoun J (2015) Lithium transport properties in $\text{LiMn}_{1-x}\text{Fe}_x\text{PO}_4$ olivine cathodes. *J Phys Chem C* 119:20855–20863
- [61] Yang K, Yu XQ, Sun JP, Li H, Huang XJ (2011) Kinetic analysis on LiFePO_4 thin films by CV, GITT, and EIS. *Electrochim Acta* 56:4869–4875
- [62] Zhu YJ, Wang CS (2010) Galvanostatic intermittent titration technique for phase-transformation electrodes. *J Phys Chem C* 114:2830–2841
- [63] Hong Y, Tang Z, Wang S, Quan W, Zhang Z (2015) High-performance LiMnPO_4 nanorods synthesized via a facile EG-assisted solvothermal approach. *J Mater Chem A* 3:10267–10274